Helicity-tunable spin Hall and spin Nernst effects in unconventional chiral fermion semimetals XY (X = Co, Rh; Y = Si, Ge)

Ting-Yun Hsieh,[1,*] Babu Baijnath Prasad,[1,2,3,*] and Guang-Yu Guo[1,3,†]

[1]*Department of Physics, National Taiwan University, Taipei 10617, Taiwan, Republic of China*

[2]*Nano Science and Technology Program, Taiwan International Graduate Program, Academia Sinica, Taipei 11529, Taiwan, Republic of China*

[3]*Physics Division, National Center for Theoretical Sciences, Taipei 10617, Taiwan, Republic of China*

(Received 16 May 2022; revised 26 August 2022; accepted 22 September 2022; published 3 October 2022)

Transition metal monosilicides CoSi, CoGe, RhSi, and RhGe in the chiral cubic B20 structure (the CoSi family) have recently been found to host unconventional chiral fermions beyond spin-1/2 Weyl fermions, and also to exhibit exotic physical phenomena such as long Fermi arc surface states, gyrotropic magnetic effect, and quantized circular photogalvanic effect. Thus, exploring novel spin-related transports in these unconventional chiral fermion semimetals may open a new door for spintronics and spin caloritronics. In this paper, we study the intrinsic spin Hall effect (SHE) and spin Nernst effect (SNE) in the CoSi family based on *ab initio* relativistic band structure calculations. First, we find that unlike nonchiral cubic metals, the CoSi family have two independent nonzero spin Hall (Nernst) conductivity tensor elements, namely, σ_{xy}^{z} and σ_{xz}^{y} (α_{xy}^{z} and α_{xz}^{y}) instead of one element. Furthermore, the SHC (σ_{xy}^{z} and σ_{xz}^{y}) and helicity of the chiral structure are found to be correlated, thus enabling SHE detection of structural helicity and also chiral fermion chirality. Second, the intrinsic SHE and SNE in some of the CoSi family are large. In particular, the calculated spin Hall conductivity (SHC) of RhGe is as large as -140 $(\hbar/\mathrm{e})(\mathrm{S/cm})$. The calculated spin Nernst conductivity (SNC) of CoGe is also large, being -1.3 $(\hbar/\mathrm{e})(\mathrm{A/m\ K})$ at room temperature. Due to their semimetallic nature with low electrical conductivity, these topological semimetals may have large spin Hall and spin Nernst angles, being comparable to that of platinum metal. The SHC and SNC of these compounds can also be increased by raising or lowering the chemical potential to, e.g., the topological nodes, via either chemical doping or electrical gating. Our findings thus indicate that transition metal monosilicides of the CoSi family not only would provide a material platform for exploring novel spin transports and exotic phenomena in unconventional chiral fermion semimetals, but also could be promising materials for developing better spintronic and spin caloritronic devices.

DOI: 10.1103/PhysRevB.106.165102

I. INTRODUCTION

Spin current generation and manipulation are key issues in spintronics. The spin Hall effect (SHE) [1–14], i.e., generation of pure transverse spin current in a nonmagnetic material with relativistic electron interaction (spin-orbit coupling) by an electric field, was first proposed by Dyakonov and Perel in 1971 [1]. It requires neither an applied magnetic field nor a magnetic material to produce a pure spin current [2–11], thus offering an important advantage for the fabrication of low-power-consumption spintronic devices [13,14] such as spin-orbit torque switching-based nanodevices [12]. Large intrinsic SHE has been predicted and also observed in several 5d transition metals such as platinum because of their strong spin-orbit coupling (SOC) [9–14]. More recently, it was predicted that transverse spin current could also be generated in a nonmagnetic material by applying a temperature gradient (∇T) instead of an electric field E [15]. This thermoelectric analog of SHE is known as the spin Nernst effect (SNE) and would make spintronic devices powered by heat possible, leading to a new field called spin caloritronics [16]. Large SNE was recently observed in platinum and tungsten metals [17,18].

In the past few years, the study of SHE [19–28] and SNE [22,26] in so-called topological semimetals has attracted considerable attention. In high-energy physics, the standard model predicts three kinds of fermionic particles in the Universe, namely, Dirac, Weyl, and Majorana fermions, on the basis of the Poincaré group. However, only Dirac fermions have been captured so far. Interestingly, in condensed matter physics, a variety of fermionic quasiparticles have been realized in topological semimetals which are not constrained by the Poincaré symmetry [29–32]. In a Dirac semimetal, which is usually a nonmagnetic centrosymmetric crystal, the bulk band structure hosts fourfold degenerate band crossing points (called Dirac points) with linearly dispersed excitations described by the 4×4 Dirac Hamiltonian [29]. When the spatial inversion symmetry is broken, as in a Weyl semimetal (WSM), a Dirac point is split and produces a pair of twofold stable band crossing points (called Weyl points) with linearly dispersed excitations described by the 2×2 Weyl Hamiltonian [29]. A pair of Weyl points behaves as a pair of

*These authors contributed equally to this work.
†gyguo@phys.ntu.edu.tw

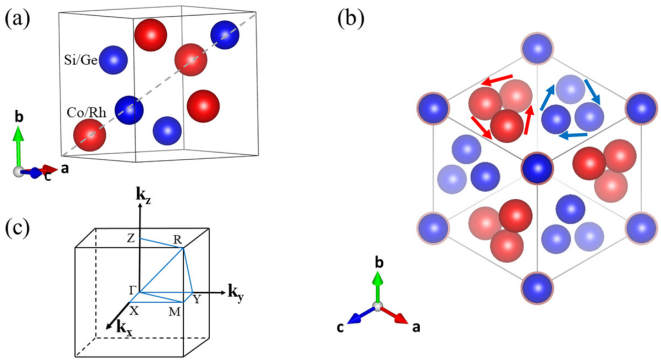

FIG. 1. Cubic B20 chiral crystal structure of the CoSi family. (a) Cubic primitive unit cell. (b) Top view along the [111] direction [the dashed gray line in (a)] of the crystal structure (2×2×2 supercell). Here the transparency of the atoms denotes the depth of the atomic positions from top to bottom. The red and blue arrows indicate the right-handed and left-handed helicity (chirality) of the Co/Rh and Si/Ge atoms, respectively. In this paper, the helicity of the Co/Rh atoms is used to define the chirality of the crystal because the energy bands near the Fermi level are dominated by Co/Rh *d* orbitals. (c) The corresponding cubic Brillouin zone.

monopoles of Berry curvature in momentum space and carries opposite chiral charges (Chern numbers) of ±1 [29]. Since the SHE could be considered as derived from the interplay of the spin-momentum locking and large Berry curvature of the electronic bands near the Weyl points [14,33], one could expect large intrinsic SHE in Weyl semimetals (WSMs) [20]. Indeed, the TaAs family of Weyl semimetals (WSMs) was predicted to exhibit large SHE [20]. More recently, large SHE was observed in WSM WTe_2 [23–25].

Transition metal monosilicides CoSi, CoGe, RhSi, and RhGe (known as the CoSi family) crystallize in a chiral cubic lattice [34–38] (see Fig. 1). Interestingly, new types of chiral fermions beyond spin-1/2 Weyl fermions, such as spin-3/2 and spin-1 chiral fermions, have recently been discovered in structurally chiral crystals including the CoSi family considered here [30–32,39]. Unlike spin-1/2 Weyl fermions, spin-3/2 and spin-1 fermionic quasiparticles have no counterpart in high-energy physics, and thus are called unconventional (or multifold) chiral fermions. Unlike Weyl points, multifold chiral fermion nodes sit on high-symmetry points and lines in the Brillouin zone with their chiral charges being larger than ±1. Furthermore, two partners of a pair of nodal points can be located at two different energy levels [30–32,39]. As a result, unconventional chiral fermion semimetals were predicted to exhibit exotic physical phenomena such as long Fermi arc surface states [31,32,40], gyrotropic magnetic effect [41], and quantized circular photogalvanic effect [42].

Therefore, we may expect that the CoSi family would exhibit novel spin transport phenomena and thus become useful materials for spintronic and spin caloritronic devices. In nonchiral cubic crystals such as platinum and tungsten metals, the spin Hall conductivity (SHC) tensor has only one independent nonzero element (σ^z_{xy}), and $\sigma^z_{yx} = -\sigma^z_{xy}$ [10]. In contrast, because of the absence of the chiral symmetry, the SHC tensor of the CoSi family has two independent nonzero elements and, in general, $\sigma^z_{yx} = \sigma^y_{xz} \neq -\sigma^z_{xy}$, as reported below in Sec. III B. Among the CoSi family, only the SHE in CoSi was recently studied by combining experiments and first-principles calculations, and the SHC (σ^z_{xy}) was found to be quite large [28]. However, the other SHC element σ^y_{xz} was not considered in Ref. [28]. As reported below in Sec. III B, the knowledge of both independent nonzero SHC tensor elements would allow us to determine the helicity of the chiral fermions in the CoSi family and also to identify their structural chirality. Note that detection of the relationship between chirality of chiral fermions and structural chiral crystals has currently attracted considerable interest [43–46].

No study of the SNE in the CoSi family has been reported. We notice that members of the CoSi family are semimetals with large Seebeck coefficient and thermopower and thus have been extensively studied as thermoelectric materials for many years [47–50]. For example, CoSi and CoGe have a large negative Seebeck coefficient of about −80 μV/K [49,50]. Thus, one could expect the CoSi family to be exploited for thermal spin current generation via SNE. Furthermore, recent first-principles calculations [28] showed that the energy derivative of the SHC $\sigma^z_{xy}(E_F)'$ at the Fermi level (E_F) in CoSi is very large. This further suggests that large SNE could occur in the CoSi family because the Mott relation [see Eq. (4)] says that the spin Nernst conductivity (SNC) is proportional to $\sigma^z_{xy}(E_F)'$ [22,33].

In this article, therefore, we present a systematic study of the SHE and SNE as well as topological aspects of the band structure of these unconventional chiral fermion compounds CoSi, CoGe, RhSi, and RhGe by performing *ab initio* density functional theory (DFT) calculations. The rest of this article is organized as follows. In Sec. II, we introduce the crystal structure of the CoSi family, followed by a brief description of the (spin) Berry phase formalism for calculating the intrinsic SHC and SNC along with the computational details. The main results are presented in Sec. III, which consists of four sections. In Sec. III A, we first analyze the topological properties of the calculated relativistic band structures and density of states of the CoSi family. Calculated SHC and SNC for the CoSi family are presented in Secs. III B and III C, respectively, where we also compare our results with that in other known materials. Finally, an analysis of the *k*-resolved spin Berry curvature is presented in Sec. III D in order to understand the origins of the calculated intrinsic SHC and SNC of the CoSi family. Finally, we summarize the conclusions drawn from this work in Sec. IV.

II. THEORY AND COMPUTATIONAL DETAILS

The CoSi family crystalizes in the simple cubic *B*20-type structure with space group $P2_13$ (see Fig. 1) [34,35]. As mentioned before, this structure is structurally chiral, and when viewed along the [111] axis, it can be either a right-handed crystal (RHC) or a left-handed crystal (LHC) [see Fig. 1(b)]. Nevertheless, the structural chirality of a grown crystal could not be prespecified and it would depend perhaps on the specific growth process. Interestingly, based on our calculated SHCs, presented in the next section, we find that the crystal structures of CoSi reported, respectively, in Refs. [34] and [35] have the opposite chiralities. Nevertheless, both RHC and

LHC structures have the same band dispersions. Furthermore, as reported in Sec. III, their SHC and SNC tensors are related although they are different. Therefore, in this study, we focus on the right-handed crystals [34] unless stated otherwise. In the present *ab initio* calculations, we use the experimental lattice constants as well as measured atomic positions for all four considered compounds [34,36–38].

Our self-consistent electronic structure calculations are based on the density functional theory (DFT) with the generalized gradient approximation (GGA) [51]. The accurate projector augmented-wave method [52], as implemented in the Vienna Ab Initio Simulation Package (VASP) [53,54], is used. The valence electronic configurations of Co, Rh, Si, and Ge taken into account in the present *ab initio* study are $3d^8 4s^1$, $4d^8 5s^1$, $3s^2 3p^2$, and $3d^{10} 4s^2 4p^2$, respectively. A large plane-wave energy cutoff of 400 eV is used throughout. In the self-consistent electronic structure calculations, a Γ-centered k-point mesh of $16 \times 16 \times 16$ is used in the Brillouin zone (BZ) integration by the tetrahedron method [55,56]. However, for the density of states (DOS) calculations, a denser k-point grid of $24 \times 24 \times 24$ is adopted.

The intrinsic SHC is calculated via the Kubo formula in the clean limit ($\omega = 0$) within the elegant Berry-phase formalism [10,33,57]. Within this formalism, the SHC ($\sigma_{ij}^s = J_i^s / E_j$) is given by the BZ integration of the spin Berry curvature for all the occupied bands below the Fermi level E_F [10],

$$\sigma_{ij}^s = e \sum_n \int_{BZ} \frac{d\mathbf{k}}{(2\pi)^3} f_{\mathbf{k}n} \Omega_{ij}^{n,s}(\mathbf{k}), \tag{1}$$

$$\Omega_{ij}^{n,s}(\mathbf{k}) = \sum_{n' \neq n} \frac{2\mathrm{Im}[\langle \mathbf{k}n | \{\tau_s, v_i\}/4 | \mathbf{k}n' \rangle \langle \mathbf{k}n' | v_j | \mathbf{k}n \rangle]}{(\epsilon_{\mathbf{k}n} - \epsilon_{\mathbf{k}n'})^2 + (\eta)^2}, \tag{2}$$

where $f_{\mathbf{k}n}$ is the Fermi distribution function, and $\Omega_{ij}^{n,s}(\mathbf{k})$ is the spin Berry curvature for the nth band at $\mathbf{k}$ with $i, j \in (x, y, z)$ and $i \neq j$. Also, τ_s, v_i (v_j), and η denote the Pauli matrix, velocity operator, and fixed smearing parameter, respectively. J_i^s is the ith component of the spin current density J^s, E_j is the jth component of the electric field E, and s is the spin direction, respectively. Once the SHC is calculated, the SNC ($\alpha_{ij}^s = -J_i^s / \nabla_j T$) is obtained by an energy integration of the calculated SHC [33],

$$\alpha_{ij}^s = \frac{1}{e} \int_{-\infty}^{\infty} d\varepsilon \frac{\partial f}{\partial \varepsilon} \sigma_{ij}^s(\varepsilon) \frac{\varepsilon - \mu}{T}, \tag{3}$$

where μ is the chemical potential.

Since a large number of k points are required to get accurate SHC and SNC, we use the efficient Wannier function interpolation scheme [58,59] based on the maximally localized Wannier functions (MLWFs) [60] as implemented in the WANNIER90 package [61]. Since the energy bands around the Fermi level are mainly dominated by transition metal d_{xy} orbitals, eight d_{xy} orbital MLWFs per unit cell of the CoSi family are constructed by fitting to the *ab initio* relativistic band structure in the energy window from −0.5 to 0.5 eV around E_F. The band structure obtained by the Wannier interpolation for the CoSi family agrees well with that from the *ab initio* calculation, as can be seen in Fig. S1 in the Supplemental Material (SM) [62]. The SHC for all four compounds of the CoSi family is then evaluated by taking a very dense k mesh of $200 \times 200 \times 200$, with a $5 \times 5 \times 5$ adaptive refinement scheme. Test calculations using several different sets of k meshes show that the calculated SHC and SNC for all four considered compounds of the CoSi family converge within a few percent.

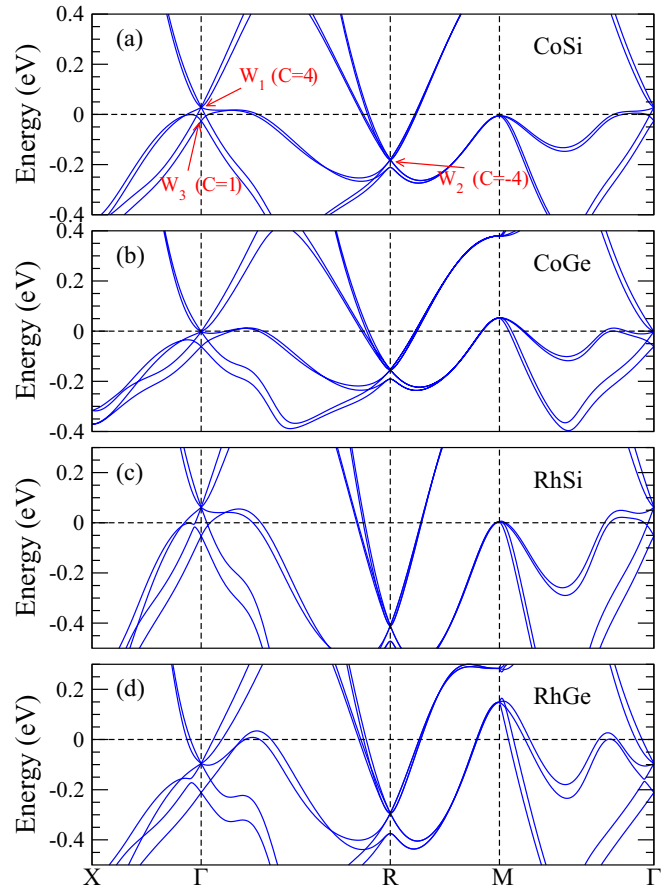

FIG. 2. Relativistic band structures of (a) CoSi, (b) CoGe, (c) RhSi, and (d) RhGe. Here, the Fermi level is at zero energy. In (a), the topological nodes at the Γ and R points are labeled in red together with their Chern numbers (chiral charges).

III. RESULTS AND DISCUSSION

A. Electronic structure

We find that all four considered compounds of the CoSi family possess a nonmagnetic ground state. The calculated relativistic band structures and density of states (DOS) of the CoSi family are shown in Figs. 2 and 3, respectively. We also calculate the scalar-relativistic band structures of the CoSi family (i.e., without including the SOC), as shown in Fig. S2 in the SM [62]. Compared with scalar-relativistic bands (Fig. S2 in the SM [62]), relativistic bands (Fig. 2) are split along the high-symmetry points and lines in the BZ. In particular, at the Γ point, the sixfold band crossing near E_F in the scalar-relativistic band structures (Fig. S2 in the SM [62]) is split and becomes two band crossing points at two different energy levels with fourfold and twofold degeneracy in the vicinity of the Fermi level when the SOC is included (see Fig. 2 and also Figs. S3–S6 in the SM [62]). The calculated Chern numbers of the fourfold (W_1) and twofold

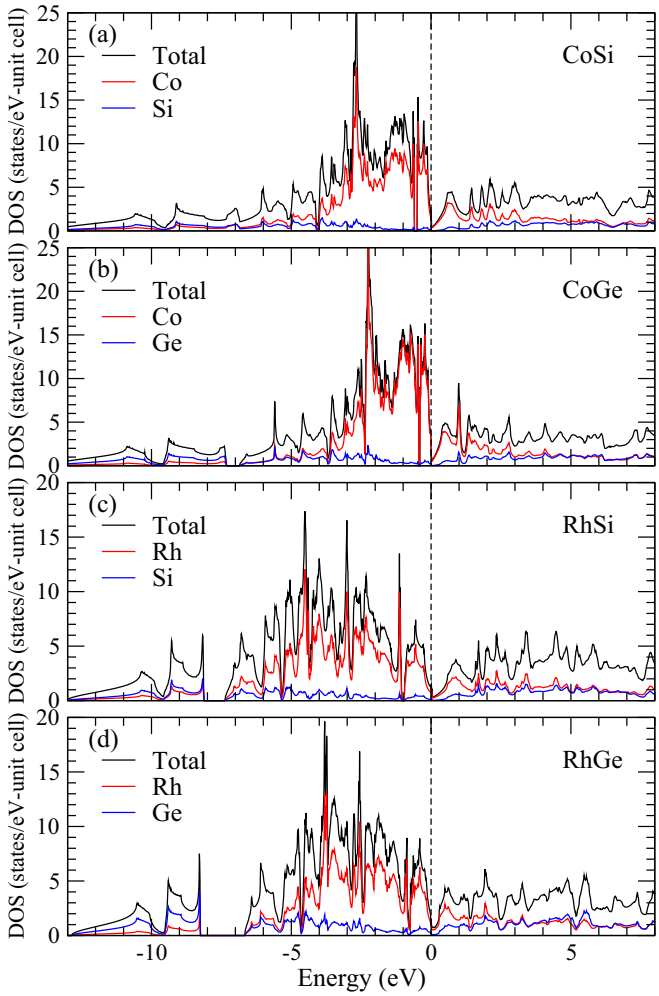

FIG. 3. Total and atom-decomposed density of states (DOS) of (a) CoSi, (b) CoGe, (c) RhSi, and (d) RhGe. Here, the Fermi level is at zero energy.

(W_3) degenerate band crossing points are +4 and +1 [see Fig. 2(a)], respectively. Therefore, nodal points W_1 and W_3 are right-handed chiral fermion nodes with chiral charges of +4 and +1, respectively. At the R point, the eightfold band crossing below E_F in the scalar-relativistic band structures (Fig. S2 in the SM [62]) also splits. This results in two band crossing points, i.e., one band crossing (W_2) with sixfold degeneracy having a Chern number of −4 (i.e., left-handed chiral fermion node) and the other band crossing below W_2 in the relativistic case (see Fig. 2). While the twofold band crossing W_3 with Chern number of +1 is the conventional Weyl fermion node, the fourfold band crossing W_1 at the Γ and sixfold band crossing W_2 at the R point are known as spin-3/2 Rarita-Schwinger-Weyl (RSW) fermion and spin-1 double Weyl fermion nodes, respectively [30–32]. Unlike Weyl fermions, the spin-3/2 RSW fermions and spin-1 double Weyl fermions have no counterpart in high-energy physics. Therefore, they are often called unconventional (i.e., beyond the standard model) chiral fermions [30–32,40]. Interestingly, the nodes at the Γ point are at close vicinity to E_F (see Table S1 in the SM [62] for detailed values), and thus may significantly affect the spin transport properties such as SHC and SNC. The nodes at the R point, however, lie further below E_F for the investigated compounds, and thus their impact can be expected to be much smaller. The origin of unconventional chiral fermions in the studied compounds can be understood by symmetry analysis as described in Refs. [31] and [32].

Figure 3 shows the total and atom-decomposed density of states (DOS) as a function of energy (E) of the CoSi family. Total and atomic orbital-decomposed DOS spectra are also shown in Fig. S7 in the SM [62]. All four investigated compounds have a pseudogap at the Fermi level and thus have a low DOS value at E_F (Fig. 3 and Fig. S7 in the SM [62]), as can be expected from a semimetal. Interestingly, in CoSi and CoGe, the DOS increases sharply as E is lowered below E_F, but increases much less dramatically if E is raised above E_F. This strong electron-hole asymmetry in the DOS in the vicinity of E_F was attributed to cause the large negative Seebeck coefficient of about $-80\ \mu$V/K in CoSi and CoGe [50]. From Fig. 3 (as well as Fig. S7 in the SM [62]), it is clear that Co (Rh) d orbitals give the main contribution to the DOS across a wide energy range around E_F with a minor contribution from Co (Rh) p orbitals and Si (Ge) p orbitals. However, Si (Ge) s orbitals are dominant for the lower-energy bands below −7.4 eV (see Fig. 3 and Fig. S7 in the SM [62]).

B. Spin Hall effect

From Eq. (1), it is clear that the SHC of a material is a third-rank tensor (σ^s_{ij}; $s, i, j = x, y, z$), and thus has 27 tensor elements in total. Nevertheless, due to the constraint of the crystalline symmetry of the material, many of these tensor elements become zero [64]. Indeed, due to the high symmetry of the cubic $B20$-type structure, the CoSi family has only two independent nonzero tensor elements, namely, σ^z_{xy} and σ^z_{yx} [64]. Other nonzero elements are related to these two elements by $\sigma^x_{yz} = \sigma^y_{zx} = \sigma^z_{xy}$ and $\sigma^y_{xz} = \sigma^x_{zy} = \sigma^z_{yx}$ (see Table I). Note that for nonchiral cubic materials such as Pt metal [10], there is only one independent nonzero element, i.e., σ^z_{xy}, and $\sigma^z_{yx} = -\sigma^z_{xy}$. The CoSi family has two independent nonzero tensor elements because their structural chiral symmetry is broken, as mentioned above in Sec. II. Therefore, the magnitude of $(\sigma^z_{xy} + \sigma^z_{yx})$ is a measure of the structural chirality of the CoSi family. Following the convention [64], we will focus on σ^z_{xy} and σ^y_{xz} instead of σ^z_{xy} and σ^z_{yx} below. In Table II, we list the calculated independent nonzero elements of the SHC tensor for the CoSi family. The σ^z_{xy} and σ^y_{xz} of recently studied Weyl semimetal TaAs [20] and Dirac line-node semimetal ZrSiS [22], as well as the σ^z_{xy} of platinum metal [10,17], are also listed in Table II for comparison.

It is well known that the handedness of a chiral crystal can be transformed simply by a spatial inversion (parity) operation ($\mathcal{P}$), e.g., from the RHC to LHC. Interestingly, here we discover that there are many other operations which can also change the handedness of the chiral crystal from the RHC to LHC, or vice versa. For example, for the CoSi family, we find that there are nine nonsymmorphic glide operations, each consisting of a mirror reflection and a fractional lattice translation [e.g., $(M_{1\bar{1}0}|\frac{3}{4}\frac{3}{4}\frac{3}{4})$], which would transform the handedness from the RHC to LHC, as listed in Table S2 in the SM [62]. For clarity, let us label the LHC obtained from the RHC through a parity operation LHC-$\mathcal{P}$, and the LHC resulted

TABLE I. $P2_13$ symmetry-imposed shape of the SHC tensor for the CoSi family in the right-handed crystal (RHC) (left column) and left-handed crystal (LHC-M) (right column). Here, the LHC-M is obtained from the RHC via a nonsymmorphic operation involving mirror reflection M, e.g., $(M_{1\bar{1}0}|\frac{3}{4}\frac{3}{4}\frac{3}{4})$ (see Table S2 in the SM [62]). Clearly, σ^z_{xy}(LHC-M) $= -\sigma^y_{xz}$(RHC) and σ^y_{xz}(LHC-M) $= -\sigma^z_{xy}$(RHC). In contrast, for the LHC obtained from the RHC through a parity operation $\mathcal{P}$ (i.e., LHC-$\mathcal{P}$), the nonzero elements of the SHC tensor are the same as that of the RHC (see the main text). Note that there are only two inequivalent nonzero elements (i.e., σ^z_{xy} and σ^y_{xz}) and that the shape of the SNC tensor is the same as that of the SHC.

SHC (RHC)						SHC (LHC-M)					
$\underline{\sigma^x}$			$\underline{\sigma^y}$			$\underline{\sigma^z}$			$\underline{\sigma^x}$			$\underline{\sigma^y}$			$\underline{\sigma^z}$		
$\begin{pmatrix}0&0&0\\0&0&\sigma^z_{xy}\\0&\sigma^y_{xz}&0\end{pmatrix}$			$\begin{pmatrix}0&0&\sigma^y_{xz}\\0&0&0\\\sigma^z_{xy}&0&0\end{pmatrix}$			$\begin{pmatrix}0&\sigma^z_{xy}&0\\\sigma^y_{xz}&0&0\\0&0&0\end{pmatrix}$			$\begin{pmatrix}0&0&0\\0&0&-\sigma^y_{xz}\\0&-\sigma^z_{xy}&0\end{pmatrix}$			$\begin{pmatrix}0&0&-\sigma^z_{xy}\\0&0&0\\-\sigma^y_{xz}&0&0\end{pmatrix}$			$\begin{pmatrix}0&-\sigma^y_{xz}&0\\-\sigma^z_{xy}&0&0\\0&0&0\end{pmatrix}$		

from the RHC via a nonsymmorphic operation involving a mirror reflection LHC-M. Furthermore, we find that the SHC tensor elements for the RHC and LHC-$\mathcal{P}$ crystals are the same. This can be seen as follows. Equation (1) shows that the SHC is given by the sum of spin Berry curvature over the BZ. For a system where the spin is a good quantum number, $\Omega^{n,k}_{ij} = s_k\Omega_{ij}$ [20]. Thus, the spin Berry curvatures and hence the SHC would remain unchanged under parity because both the Berry curvatures (Ω_{xy} and Ω_{xz}) and spin operators (S^z and S^y) are pseudovectors and thus even under parity. To verify this conclusion, we perform explicit calculations of the SHC for both RHC and LHC-$\mathcal{P}$ of CoSi, and indeed find that the calculated σ^z_{xy} and σ^y_{xz} values for these two structures are identical (within the numerical uncertainties).

Surprisingly, we find that the SHC tensor elements for the RHC and LHC-M structures are different. Nevertheless, they are connected via simple relations σ^y_{xz}(LHC-M) $= -\sigma^z_{xy}$(RHC) and σ^z_{xy}(LHC-M) $= -\sigma^y_{xz}$(RHC) (see Table I). To understand the origin of these SHC relations, let us take the nonsymmorphic operation $(M_{1\bar{1}0}|\frac{3}{4}\frac{3}{4}\frac{3}{4})$ as an example. As the mirror reflection $(M_{1\bar{1}0})$ changes the Berry curvature Ω_{xz} to Ω_{yz} and spin operator S^y to $-S^x$, we get relation Ω^y_{xz}(RHC) $= -\Omega^x_{yz}$(LHC-M) for the spin Berry curvature. This results in σ^y_{xz}(RHC) $= -\sigma^x_{yz}$(LHC-M) $= -\sigma^z_{xy}$(LHC-M), i.e., σ^z_{xy}(LHC-M) $= -\sigma^y_{xz}$(RHC), as mentioned earlier. We notice that the crystal structures of CoSi reported in Refs. [34] and [35] have the opposite chiralities. Furthermore, the structure reported by Demchenko *et al.* [35] is nearly the same as the LHC-M of the crystal structure reported by Kavich *et al.* [34] (with a measure of similarity, $\Delta = 0.005$ [67]) (see, also, Table S3 in the SM [62]). Therefore, to verify these relations, we again perform explicit calculations of the SHC for these structures reported by [34] (RHC) and [35] (LHC-M), and the results are shown in Fig. S10 in the SM [62]. Figure S10 in the SM [62] shows that indeed σ^z_{xy}(LHC-M) $\approx$ -σ^y_{xz}(RHC) and σ^y_{xz}(LHC-M) $\approx$ -σ^z_{xy}(RHC). The small discrepancies are due to the slight

TABLE II. Calculated spin Hall conductivity (σ^z_{xy} and σ^y_{xz}), and spin Nernst conductivity (α^z_{xy} and α^y_{xz}) at temperature $T = 300$ K of the CoSi family. Previous results for Weyl semimetal TaAs, Dirac line-node semimetal ZrSiS, and heavy Pt metal are also listed for comparison. To estimate the spin Hall (Nernst) angle $\Theta_{sH} = 2\sigma^s/\sigma^c_{xx}$ [$\Theta_{sN} = 2\alpha^s/\alpha_{xx} = 2\alpha^s/(S_{xx}\sigma^c_{xx})$], we also list experimental electrical conductivity σ^c_{xx} and Seebeck coefficient S_{xx} values as well as the estimated Θ_{sH} and Θ_{sN} here.

System	σ^c_{xx} (S/cm)	S_{xx} (μV/K)	σ^z_{xy} ($\hbar$/e)(S/cm)	Θ^z_{sH} (%)	σ^y_{xz} ($\hbar$/e)(S/cm)	Θ^y_{sH} (%)	α^z_{xy} ($\hbar$/e)(A/m-K)	Θ^z_{sN} (%)	α^y_{xz} ($\hbar$/e)(A/m-K)	Θ^y_{sN} (%)
CoSi	5200[c]	-81[c]	-63, 52[j]	-2.4	-66	-2.5	0.42	-2.0	-1.00	4.7
CoGe	4589[d]	-82[d]	-131	-5.7	-21	-0.9	0.06	-0.3	-1.25	6.6
RhSi	3571[e]	-25[h]	-122	-6.8	11	0.6	0.14	-3.1	-0.65	14.6
RhGe	4130[f]	-25[f]	-139	-6.7	103	5.0	-0.64	12.4	-0.19	3.7
TaAs[a]			-781		357					
ZrSiS[b]			79		-280		0.60		0.52	
Pt	20833[g]	-3.7[i]	2139[k]	10[g]			-1.09[l],-1.57[i]	-20[i]		

[a] *Ab initio* calculation [20];
[b] *Ab initio* calculation [22];
[c] Transport experiment [49];
[d] Transport experiment [50];
[e] Transport experiment [65];
[f] Transport experiment [47];
[g] Transport experiment [66];
[h] Assumed the same value as RhGe from [47];
[i] Experiment at 255 K [17];
[j] *Ab initio* calculation [28];
[k] *Ab initio* calculation [10];
[l] *Ab initio* calculation [57].

differences in the atomic positions in these crystalline structures [34,35] (see, also, Table S3 in the SM [62]). This shows that the SHC can be used to identify the handedness (chirality) for the crystal structure of the CoSi family as well as other chiral materials. Here we mention two cases to demonstrate how measuring the SHC tensor elements can help determine the handedness (chirality) of a structurally chiral crystal. First, let us assume that both the SHC tensor elements (σ^z_{xy} and σ^y_{xz}) are of the same sign, e.g., negative as in the case of RHC CoSi and CoGe at the Fermi level (see Table II). Now if one observes a positive sign for these two elements for the same crystal with unknown handedness, using our relations as shown in Table I for the RHC and LHC-M, one can conclude that the unknown handedness crystal is LHC-M. Second, when both the SHC tensor elements (σ^z_{xy} and σ^y_{xz}) are of the opposite sign [as in the case of RhSi and RhGe at the Fermi level (see Table II); RHC], one needs to consider the magnitude of both SHC tensor elements as well to determine the handedness of the same crystal. Note that the two SHC tensor elements of RhSi and RhGe differ quite a lot in terms of magnitude and can be used to determine the handedness. Furthermore, since the chirality [or the sign of the Chern number (chiral charge)] of a chiral fermion node is determined by the structural chirality (see Table S1 in the SM [62]), the calculated SHC can also be used to identify the helicity (chirality) of the chiral fermions in the CoSi family and also in other chiral lattices. Note that detection of the relationship between the chirality of chiral fermions and structurally chiral crystals is a topic of considerable current interest [43–46]. Nevertheless, as mentioned above, we will focus on the CoSi family in the RHC structure in the following.

The calculated SHC values for the four investigated compounds are listed in increasing order of their SOC strength in Table II. The calculated σ^z_{xy} for CoSi is the smallest and that of RhGe is the largest, a trend which apparently follows the increasing order of the SOC in the CoSi family. Nevertheless, an even more pronounced trend is present in the calculated σ^y_{xz} values. Furthermore, the sign of σ^y_{xz} for RhSi and RhGe is opposite to that for CoSi and CoGe. RhGe has the largest σ^z_{xy} of -139 $(\hbar/\mathrm{e})(\mathrm{S/cm})$, being larger than that [79 $(\hbar/\mathrm{e})(\mathrm{S/cm})$] of Dirac line-node semimetal ZrSiS [22], but significantly smaller than that [-781 $(\hbar/\mathrm{e})(\mathrm{S/cm})$] of archetypal Weyl semimetal TaAs [20]. Nevertheless, the σ^z_{xy} of RhGe is about 20 times larger than the σ^z_{xy} [7 $(\hbar/\mathrm{e})(\mathrm{S/cm})$] of Weyl semimetal NbP [20]. Finally, the σ^z_{xy} value of RhGe is about 15 times smaller than that of platinum metal, which possesses the largest SHC among the transition metals.

Table II also shows a strong anisotropy of the SHC in the CoSi family. By interchanging the applied electric field and spin polarization directions simultaneously from (z, y) to (y, z), one can obtain the multifold enhancement of the SHC. Here, the first and second index in parentheses corresponds to the applied electric field and spin polarization directions, respectively. For example, the σ^z_{xy} of CoGe and RhSi is about 6 times and 11 times larger than the corresponding σ^y_{xz}, respectively. Furthermore, the signs of the SHC σ^z_{xy} and σ^y_{xz} for RhSi and RhGe also differ.

Since chiral fermion nodes W_1 at the Γ point and W_2 at the R point do not lie exactly at E_F (see Fig. 2 and Table S1 in the SM [62]), we also calculate the SHC as a function of chemical potential (μ) within the rigid-band approximation. In the rigid-band approximation, we vary only the μ while keeping the band structure fixed. The calculated SHC spectra are displayed in Figs. 4(b), 4(e), 4(h), and 5(b) for CoSi, CoGe, RhSi, and RhGe, respectively. In Table S1 of the SM [62], we also tabulate the SHC values when the chemical potential is shifted to either node W_1 at Γ or node W_2 at R. It is clear that the SHC spectra for the CoSi family show a strong dependence on μ. In particular, Fig. 4(b) shows that the magnitude of σ^y_{xz} of CoSi decreases steeply and then changes sign as μ is raised from E_F to 0.015 eV. The positive σ^y_{xz} then increases steeply as μ further increases until μ is above node W_1. As suggested earlier in Ref. [28], this rapid change of the magnitude and also the sign of σ^y_{xz} could be a characteristic behavior of the SHC in the vicinity of a spin-3/2 chiral fermion node. Indeed, this pronounced behavior also shows up in the σ^y_{xz} spectrum of CoGe around the spin-3/2 chiral fermion node W_1 at Γ [see Fig. 4(e)]. This rapid change of σ^y_{xz} in CoSi and CoGe can also be seen near spin-1 double Weyl fermion node W_2 at R, except the sign change occurs well below W_2 (about 0.25 eV lower). Nevertheless, the σ^y_{xz} spectrum of RhGe is rather flat in

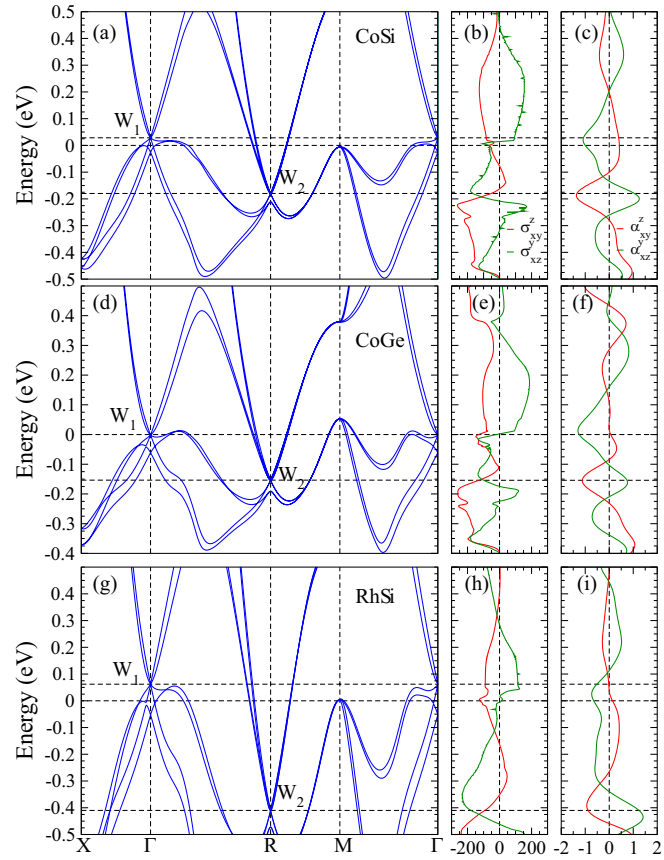

FIG. 4. (a), (d), (g) Relativistic band structure, (b), (e), (h) spin Hall conductivity (σ^z_{xy} and σ^y_{xz}) as a function of chemical potential (μ), and (c), (f), (i) spin Nernst conductivity (α^z_{xy} and α^y_{xz}) at $T =$ 300 K as a function of μ for (a)–(c) CoSi, (d)–(f) CoGe, and (g)–(i) RhSi. Here, W_1 and W_2 denote the spin-3/2 chiral fermion node at Γ and spin-1 double Weyl node at R, respectively. The Fermi level is at zero energy, and the unit of the SHC [SNC] is $(\hbar/\mathrm{e})(\mathrm{S/cm})$ $[(\hbar/\mathrm{e})(\mathrm{A/m\ K})]$.

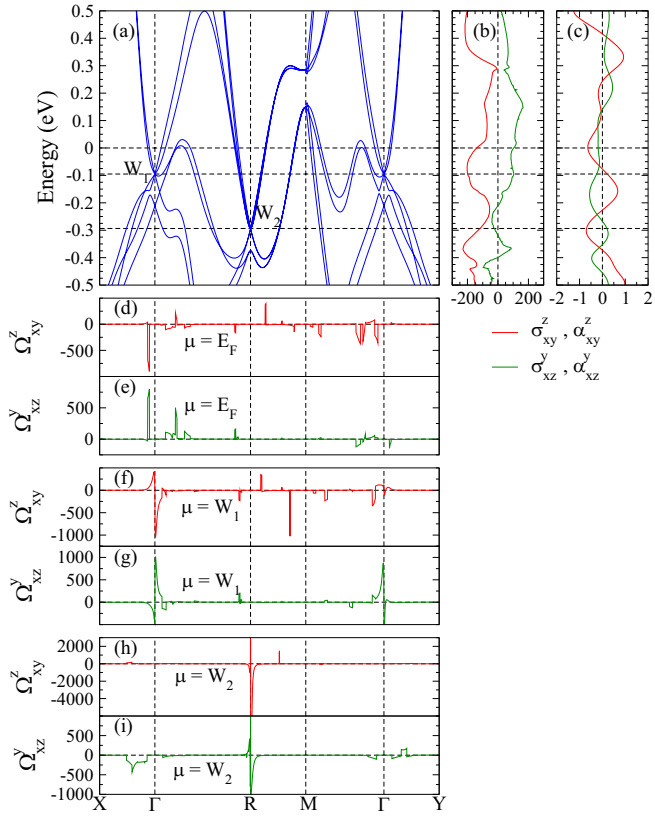

FIG. 5. RhGe. (a) Relativistic band structure; (b) spin Hall conductivity (σ^z_{xy} and σ^y_{xz}) as a function of chemical potential (μ); (c) spin Nernst conductivity (α^z_{xy} and α^y_{xz}) at $T = 300$ K as a function of μ; (d), (f), and (h) spin Berry curvature (SBC) Ω^z_{xy}; as well as (e), (g), and (i) SBC Ω^y_{xz} for $\mu = E_F$, $\mu = \mathrm{W}_1$, and $\mu = \mathrm{W}_2$, respectively, along the high-symmetry lines in the Brillouin zone. Here, W_1 and W_2 denote the spin-3/2 chiral fermion node at Γ and spin-1 double Weyl node at R, respectively. In (a)–(c), the Fermi level is at zero energy, and the unit of the SHC [SNC] is $(\hbar/\mathrm{e})(\mathrm{S/cm})$ [$(\hbar/\mathrm{e})(\mathrm{A/m\,K})$]. In (d)–(i), the unit of SBC is Å^2.

the vicinity of W_1 at Γ [see Fig. 5(b)]. Furthermore, this steep slope and sign change of σ^y_{xz} around W_1 is absent in the σ^z_{xy} spectrum of the CoSi family. Consequently, this indicates that the pronounced feature of σ^y_{xz} found near node W_1 in CoSi and CoGe may not be universal for all spin-3/2 chiral fermions.

Other prominent changes due to the variation of the μ are as follows. The σ^y_{xz} of RhSi can be increased by a factor of about 10 by slightly increasing the μ from E_F to node W_1 at 0.06 eV (see Fig. 4(h) and Table S1 in the SM [62]). This can be easily realized via electron doping of merely 0.02 e/f.u. Also, σ^y_{xz} of CoGe could be enhanced from -21 $(\hbar/\mathrm{e})(\mathrm{S/cm})$ to -98 $(\hbar/\mathrm{e})(\mathrm{S/cm})$ by lowering the μ to nodal point W_2 at -0.15 eV (see Fig. 4(e) and also Table S1 in the SM [62]). This can be achieved via hole doping of 0.27 e/f.u. Furthermore, σ^z_{xy} of CoGe and RhGe could reach a very large value of -260 $(\hbar/\mathrm{e})(\mathrm{S/cm})$ and -202 $(\hbar/\mathrm{e})(\mathrm{S/cm})$ by lowering the chemical potential to -0.19 and -0.07 eV via hole doping of 0.38 and 0.04 e/f.u., respectively [see Figs. 4(e) and 5(b)]. The above discussion clearly suggests that the SHC of the CoSi family could be tuned in both magnitude and sign by shifting the chemical potential to either the topological nodal points or other energy levels, and this could be accomplished via either chemical doping or electrical gating.

Among the members of the CoSi family, only the SHE in CoSi was recently studied experimentally using CoSi/CoFeB/MgO heterostructures by Tang *et al.* [28]. The measured values of the so-called dampinglike (σ_{DL}) and fieldlike (σ_{FL}) SHC for film thickness $t_{CoSi} = 7.2$ nm are $\sigma_{DL} = 45$ $(\hbar/\mathrm{e})(\mathrm{S/cm})$ and $\sigma_{FL} = 95$ $(\hbar/\mathrm{e})(\mathrm{S/cm})$, being in quite good agreement with our theoretical σ^z_{xy} and σ^y_{xz} values listed in Table II. Tang *et al.* also performed DFT calculations for SHC σ^z_{xy} of CoSi and their calculated σ^z_{xy} at E_F is 52 $(\hbar/\mathrm{e})(\mathrm{S/cm})$, which agrees very well with our σ^z_{xy} and σ^y_{xz} values (Table II). Interestingly, their calculated σ^z_{xy} spectrum in the vicinity of E_F (see Fig. 5(c) in [28]) looks rather similar to our σ^y_{xz} spectrum [see Fig. 4(b)], except that the two have opposite signs. In other words, σ^z_{xy} [28] $\approx -\sigma^y_{xz}$ (this work), indicating that the crystalline structure of the samples used in [28] is LHC rather than RHC considered here. Nevertheless, the σ^z_{xy} spectrum in [28] near Weyl point W_2 differs significantly from our σ^y_{xz} spectrum. These discrepancies could reflect the different computational methods and structural parameters used in the previous [28] and present studies. We note that the independent nonzero SHC element σ^y_{xz} was not studied in Ref. [28].

Finally, we notice that for the application of SHE in spintronics such as spin-orbit torque switching-based nanodevices, the crucial quantity is the so-called spin Hall angle Θ_{sH} which characterizes the charge-to-spin conversion efficiency and is given by $\Theta_{sH} = (2e/\hbar)J^s/J^c = 2\sigma^s/\sigma^c$, where J^c and σ^c are the longitudinal charge current density and conductivity, respectively (see, e.g., Refs. [68] and [66]). Therefore, although the calculated SHC values of the CoSi family are much smaller than that of 5*d* transition metals such as Pt (Table II), their spin Hall angles could be comparable to that of 5*d* transition metals [66] because topological semimetals by nature have a much smaller conductivity compared with 5*d* transition metals (Table II). For example, the spin Hall angle Θ^z_{sH} for σ^z_{xy} of RhSi and RhGe is about -7%, which is comparable to that (10%) of Pt (Table II). Therefore, we believe that this interesting finding of large spin Hall angles of the CoSi family would spur further experiments on SHE in the members of the CoSi family other than CoSi [28].

C. Spin Nernst effect

The SNC (α^s_{ij}; $s, i, j = x, y, z$) of a material is also a third-rank tensor, thus having 27 tensor elements altogether. As for the SHC, owing to the high symmetry of the cubic lattice for the CoSi family, it has only two independent nonzero tensor elements, namely, α^z_{xy} and α^y_{xz} [64] (see, also, Table I). The calculated values of these nonzero SNC elements at $T = 300$ K are listed in Table II. Remarkably, Table II indicates that the calculated value of SNC α^y_{xz} of CoGe is comparable or even larger than that (α^z_{xy}) of platinum metal (Table II). Also, α^y_{xz} of CoGe is about 2.5 times larger than α^y_{xz} of Dirac line-node semimetal ZrSiS [22] (Table II). This shows that the SNC values for the CoSi family are prominent and the CoSi family would be potential materials for spin caloritronics.

Table II indicates that the SNC of the CoSi family is strongly anisotropic, similar to their SHC. For example, the

α^z_{xy} of CoGe is about 21 times larger than α^y_{xz} (see Table II), i.e., the SNC of CoGe would be enhanced by a factor of about 21 when the applied electric field and spin polarization directions are interchanged from (y, z) to (z, y). Here the indices in the parentheses indicate the directions of the applied electric field and spin polarization, respectively. Also, the α^z_{xy} of RhGe is approximately 3.4 times larger than α^y_{xz} (Table II). A sign change in the SNC is found for CoSi, CoGe, and RhSi (Table II) when the spin polarization direction is rotated from the z axis to the y axis.

We also calculate the chemical potential (μ) dependence of the SNC at $T = 300$ K for CoSi, CoGe, RhSi, and RhGe as shown in Figs. 4(c), 4(f), 4(i), and 5(c), respectively. As for the SHC, the SNC spectra of the CoSi family also depend strongly on μ. For example, α^z_{xy} of CoGe becomes 19 times larger and also changes sign when the chemical potential is lowered to the spin-1 double Weyl fermion node at R (i.e., W_2 at -0.15 eV) (see Fig. 4(f), Table II and Table S1 in the SM [62]). This suggests that the presence of unconventional chiral fermion nodes may considerably enhance the SNE. We note that this chemical potential lowering can be realized by hole doping of 0.27 e/f.u. Also, Fig. 4(c) indicates that the α^z_{xy} of CoSi can be increased from 0.42 to -1.35 ($\hbar$/e)(A/m K) when μ is shifted to node W_2 (-0.18 eV) (see, also, Table S1 in the SM [62]). This can be achieved via hole doping of 0.25 e/f.u. Furthermore, the SNC (α^y_{xz}) of RhGe is enhanced by a factor of about 1.5 when μ drops to the level of the spin-3/2 fermion node W_1 at Γ (see Table II and Table S1 in the SM [62]), which can be achieved via hole doping of merely 0.06 e/f.u. Nevertheless, we also notice that this enhancement in SNC is absent in the α^z_{xy} of CoSi, CoGe, and RhSi at W_1 (see Fig. 4, Table II, and, also, Table S1 in the SM [62]). Also, Fig. 5(c) shows that there is no local maximum in the α^z_{xy} near W_1 in RhGe. Overall, the μ dependences of the α^z_{xy} and α^y_{xz} of CoSi, CoGe, and RhSi are rather similar (see Fig. 4). For CoSi, the α^z_{xy} decreases steadily as μ decreases and changes sign at -0.10 eV, and then reaches a negative local maximum of -1.37 ($\hbar$/e)(A/m K) at -0.19 eV [see Fig. 4(c)]. On the contrary, α^z_{xy} of RhGe increases rapidly as μ decreases, changes sign at -0.08 eV and then rises to a positive local maximum of 0.67 ($\hbar$/e)(A/m K) at -0.16 eV [Fig. 5(c)]. These remarkable tunabilities in the SNC could be observed in the CoSi family by either chemical substitution or electrical gating.

We note that Eq. (3) would be reduced to the Mott relation at the low-T limit,

$$\alpha^z_{xy}(E_F) = -\frac{\pi^2}{3}\frac{k_B^2 T}{e}\sigma^z_{xy}(E_F)', \tag{4}$$

which simply means that the SNC is proportional to the energy derivative of the SHC at E_F. This would allow us to understand the origins of the prominent features in the μ-dependent SNC spectra. For example, the large negative peak in the α^y_{xz} spectrum of CoSi in the vicinity of node W_1 is due to the positive steep slope of σ^y_{xz} near W_1 [see Figs. 4(b) and 4(c)]. This large SNC (α^y_{xz}) of -1.07 ($\hbar$/e)(A/m K) at $T = 300$ K is located at 0.02 eV, being slightly above E_F, and thus could be achieved easily via electron doping of 0.01 e/f.u. Similarly, in Figs. 4(b) and 4(c), α^z_{xy} of CoSi also has a peak value of -1.37

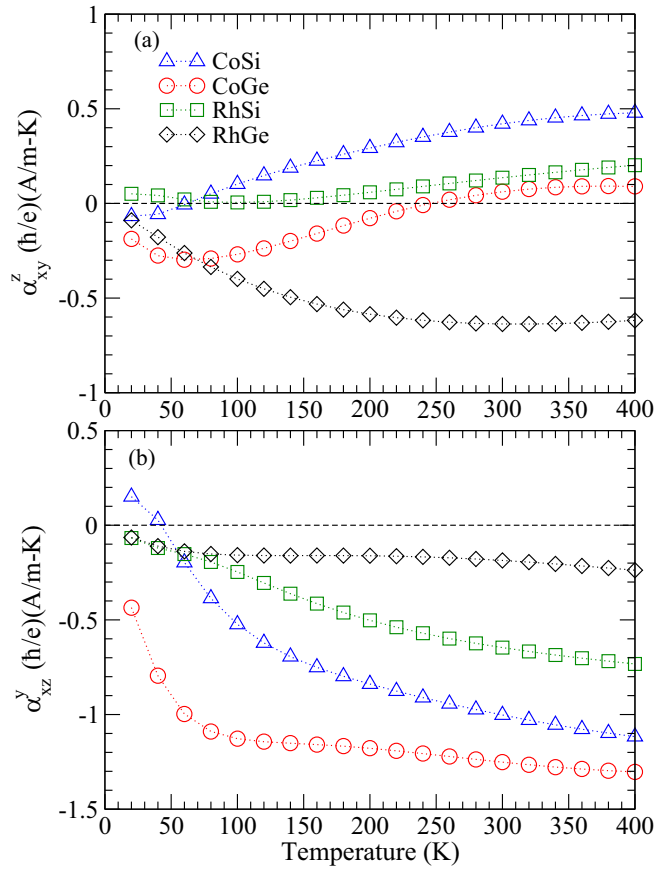

FIG. 6. Spin Nernst conductivity (a) α^z_{xy} and (b) α^y_{xz} of the CoSi family as a function of temperature T.

($\hbar$/e)(A/m K) at $T = 300$ K at spin-1 double Weyl fermion node W_2 ($\mu = -0.19$ eV) at R [Fig. 4(c)] and again this is due to the steep positive slope of σ^z_{xy} near W_2. In order to reach this energy level, however, a larger hole doping of 0.27 e/f.u. would be required. In contrast, Fig. 4(f) shows that for CoGe, α^z_{xy} is negligibly small above E_F because σ^z_{xy} is very flat in this energy range [Fig. 4(e)]. Unlike CoSi, CoGe, and RhSi, both α^z_{xy} and α^y_{xz} of RhGe are negative and α^y_{xz} of RhGe has a broad plateau of about -0.18 ($\hbar$/e)(A/m K) at $T = 300$ K from -0.05 to 0.10 eV around E_F [see Fig. 5(c)], where σ^y_{xz} increases rather slowly with μ [see Fig. 5(b)].

The temperature (T) dependence of the SNC (α^z_{xy} and α^y_{xz}) of the CoSi family is also calculated, as shown in Fig. 6. In Figs. S11 and S12 in the SM [62], we also display the T dependences of α^z_{xy}, and α^y_{xz} when μ is displaced to nodes W_1 and W_2, respectively. Figure 6(a) shows that the α^z_{xy} spectra of CoSi and RhSi have a positive value for almost the entire considered T range, which increases steadily with T and reaches 0.48 and 0.20 ($\hbar$/e)(A/m K), respectively, at $T = 400$ K. For CoGe, α^z_{xy} has a negative value of -0.30 ($\hbar$/e)(A/m K) at $T = 60$ K. As T increases, α^z_{xy} increases and changes sign at $T = 240$ K and then rises to a value of 0.09 ($\hbar$/e)(A/m K) at $T = 400$ K [see Fig. 6(a)]. However, α^z_{xy} of RhGe has a negative value in the whole T range considered here. Its magnitude increases monotonically and hits the negative maximum value of -0.64 ($\hbar$/e)(A/m K) at $T = 320$ K. It then starts to decrease as T further increases and

finally reduces to -0.62 $(\hbar/e)$(A/m K) at $T = 400$ K [see Fig. 6(a)]. In Fig. 6(b), unlike the α^z_{xy}, α^y_{xz} has a negative value for all four investigated compounds of the CoSi family in almost the entire considered temperature range. For CoSi, RhSi, and CoGe, the magnitude of α^y_{xz} increases monotonically as T increases from 50 K, and reaches the negative value of -1.12, -0.73, and -1.30 $(\hbar/e)$(A/m K), respectively, at $T = 400$ K [see Fig. 6(b)]. α^y_{xz} of RhGe shows a robust behavior with T and decreases slightly to -0.24 $(\hbar/e)$(A/m K) at $T = 400$ K, as can be seen easily in Fig. 6(b). Interestingly, for RhGe, α^z_{xy} changes sign with T when μ is shifted to node W_1 (see Fig. 6(a) and Fig. S11(a) in the SM [62]). Also, for the CoSi family, the α^z_{xy} is negative, whereas α^y_{xz} is positive for the entire considered T range when μ is lowered to node W_2 (see Fig. S12 in the SM [62]).

Finally, from the viewpoint of the application of SNE in spin caloritronics, the key quantity is the spin Nernst angle Θ_{sN} which measures the heat-to-spin conversion efficiency and is defined as $\Theta_{sN} = (2e/\hbar)J^s/J^h = 2\alpha^s/\alpha^L$, where J^h and α^L are the longitudinal heat current density and Nernst coefficient, respectively [17]. Here, $\alpha^L = S_{xx}\sigma_{xx}$, where S_{xx} is the Seebeck coefficient. Using the measured σ_{xx} and S_{xx} of the CoSi family, we estimate the Θ_{sN} values using the calculated α^s, as listed in Table II. Interestingly, we obtain the large Θ_{sN} values of 15% and 12%, respectively, for RhSi and RhGe (Table II), which are comparable to that (-20%) of Pt metal [17]. So far, no experimental or theoretical studies on the SNE in the CoSi family have been reported. We hope that this interesting finding of large spin Hall (Nernst) angles in the CoSi family, especially RhSi and RhGe, will stimulate experiments of this kind in the near future.

D. Spin Berry curvature analysis

We can see from Eq. (1) that the SHC is simply given by the summation of spin Berry curvature (SBC) of the occupied bands on all the k points in the BZ. As a result, analyzing the k-resolved SBC would help us understand the origins of the large SHC as well as SNC of the CoSi family. Table II indicates that RhGe has the largest SHC among the four considered compounds. Therefore, taking RhGe as an example, we display its calculated SBC Ω^z_{xy} in Figs. 5(d), 5(f), and 5(h), as well as Ω^y_{xz} in Figs. 5(e), 5(g), and 5(i), along the high-symmetry lines in the BZ for chemical potential $\mu = E_F$, $\mu = W_1$, and $\mu = W_2$, respectively. In order to get a clearer picture of the SBC distribution in the BZ, we also show on the k_x-k_y plane with $k_z = 0$ the contour plots of Ω^z_{xy} in Figs. 7(a)–7(c) and also of Ω^y_{xz} in Figs. 8(a)–8(c) for $\mu = E_F$, $\mu = W_1$, and $\mu = W_2$, respectively. Contour plots of Ω^z_{xy} and Ω^y_{xz} on the k_x-k_z plane with $k_y = 0.5$ for $\mu = W_2$ are also presented in Figs. 7(d) and 8(d), respectively.

For $\mu = E_F$, a sharp negative (positive) peak near the Γ point on the X-Γ line is found for Ω^z_{xy} (Ω^y_{xz}) [see Figs. 5(d) and 5(e)]. A comparison of Fig. 5(a) with Fig. S1(d) (SM [62]) indicates that the bands near E_F around this k point are slightly split when the SOC is included. As pointed out before [10], when two degenerate bands become slightly gapped by the SOC, a pair of large peaks of SBC with opposite signs would occur in the vicinity of this k point. When both bands are occupied, the contributions from these two peaks to the SHC would cancel each other. However, when E_F falls within the gap, only one peak of SBC would contribute to the SHC, thus resulting in a pronounced contribution to the SHC. Therefore, we can see that the large negative (positive) peak of Ω^z_{xy} (Ω^y_{xz}) makes a crucial contribution to the SHC, leading to the large negative σ^z_{xy} (positive σ^y_{xz}) value at E_F. These large negative Ω^z_{xy} and positive Ω^y_{xz} peaks near Γ can be seen more clearly in Figs. 7(a) and 8(a), respectively. Figure 5(d) also shows

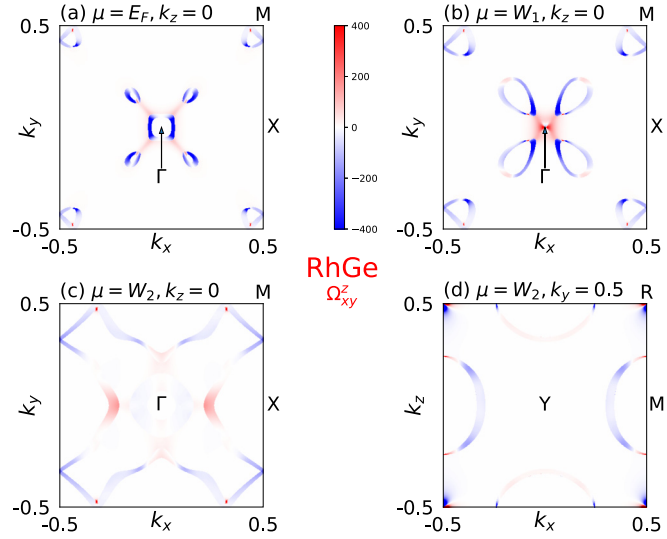

FIG. 7. **k**-resolved spin Berry curvature $\Omega^z_{xy}(\mathbf{k})$ of RhGe on the k_x-k_y plane with (a)–(c) $k_z = 0$ and also on the k_x-k_z plane with (d) $k_y = 0.5$ in the Brillouin zone. The color bar is in units of Å^2. In (a), chemical potential $\mu = E_F$; in (b), $\mu = W_1$ (spin-3/2 fermion node at Γ); in (c) and (d), $\mu = W_2$ (spin-1 double Weyl fermion node at R).

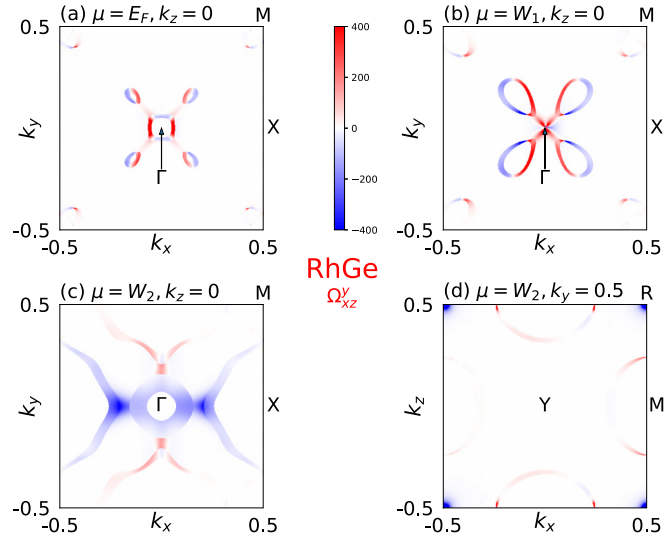

FIG. 8. **k**-resolved spin Berry curvature $\Omega^y_{xz}(\mathbf{k})$ of RhGe on the k_x-k_y plane with (a)–(c) $k_z = 0$ and also on the k_x-k_z plane with (d) $k_y = 0.5$ in the Brillouin zone. The color bar is in units of Å^2. In (a), chemical potential $\mu = E_F$; in (b), $\mu = W_1$ (spin-3/2 fermion node at Γ); in (c) and (d), $\mu = W_2$ (spin-1 double Weyl fermion node at R).

that there are less prominent negative peaks of Ω^z_{xy} along the M-Γ [see, also, Fig. 7(a)] and Γ-R lines, which should also contribute significantly to the large negative σ^z_{xy} value. Again, these large Ω^z_{xy} values originate from the small SOC-induced band splitting near E_F [see Fig. 5(a)]. Similarly, one can find rather pronounced positive Ω^y_{xz} peaks along the Γ-R line.

When the chemical potential is lowered to the spin-3/2 fermion node ($\mu = W_1$) at Γ, a large asymmetric oscillatorlike curve occurs for Ω^z_{xy} near Γ on the X-Γ-R line [see Fig. 5(f)], perhaps a unique feature of SBC near a chiral fermion node. Nevertheless, the negative peak near Γ on the Γ-R side is gigantic, which overcomes the less pronounced positive peak on the Γ-X side [Fig. 5(f)], thus resulting in the large negative σ^z_{xy} value (Table II). Of course, other pronounced negative peaks in Ω^z_{xy} such as that along the R-M-Γ line may also contribute significantly to Ω^z_{xy}. Similarly, we can also see large oscillatorlike features in Ω^y_{xz} near Γ along the X-Γ-R and M-Γ-Y lines [see Fig. 5(g)]. However, clearly, the large positive peaks on the Γ-R and Γ-M sides would overcome the smaller negative peaks of Ω^y_{xz} on the Γ-X and Γ-Y sides, thus leading to the large positive σ^y_{xz} value. When the chemical potential is further lowered to the spin-1 double Weyl fermion node ($\mu = W_2$) at R, similar oscillatory features in both Ω^z_{xy} and Ω^y_{xz} appear [see Figs. 5(h) and 5(i)]. The gigantic negative peaks of Ω^z_{xy} and Ω^y_{xz} on the R-M side [see Figs. 7(d) and 8(d)] would overwhelm the much smaller positive peaks on the R-Γ side, thereby resulting in the negative σ^z_{xy} and σ^y_{xz} values [see Fig. 5(b)]. Of course, there is also a broad negative peak of Ω^y_{xz} on the X-Γ line, which is clearly due to the large SOC-split bands [see Fig. 5(a)], and this negative peak shows up clearly as a small part of a complex negative feature in the contour plot on the k_x-k_y plane with $k_z = 0$ [see Fig. 8(c)].

IV. CONCLUSIONS

In summary, we have systematically studied the band structure topology, SHE, and SNE in the CoSi family with the chiral cubic B20 structure by performing *ab initio* relativistic band structure calculations. First, all four considered monosilicides (CoSi, CoGe, RhSi, and RhGe) are found to be nonmagnetic semimetals with unconventional chiral fermion nodes. Second, unlike nonchiral cubic metals, these monosilicides have two independent nonzero spin Hall (Nernst) conductivity tensor elements, namely, σ^z_{xy} and σ^y_{xz} (α^z_{xy} and α^y_{xz}) instead of one element. Furthermore, the SHC (σ^z_{xy} and σ^y_{xz}) and helicity of the chiral cubic structure are revealed to be correlated, thus suggesting SHE detection of structural helicity and also chiral fermion chirality. Third, the intrinsic SHE and SNE in some of the CoSi family are large. For example, the calculated SHC of RhGe is as large as -139 $(\hbar/\mathrm{e})(\mathrm{S/cm})$. The calculated SNC of CoGe at room temperature is also large, being -1.25 $(\hbar/\mathrm{e})(\mathrm{A/m\,K})$. Because of their semimetallic nature with low electrical conductivity, these topological semimetals may have large spin Hall and spin Nernst angles up to 7% and 15%, respectively, being comparable to that of platinum metal which has the largest SHC among transition metals. The SHC and SNC of these compounds can also be significantly enhanced by raising or lowering chemical potential to, e.g., a spin-3/2 chiral fermion or spin-1 double Weyl node, via either chemical doping or electrical gating. Finally, an analysis of the calculated k-resolved spin Berry curvature unveils the mechanism underlying the largeness and tunability of SHE and SNE in these materials. These interesting results thus show that transition metal monosilicides of the CoSi family not only would provide a material platform for exploring novel spin transports and exotic phenomena in unconventional chiral fermion semimetals, but also could be promising materials for developing better spintronic and spin caloritronic devices. We are sure that this work would stimulate new experiments on SHE and SNE in these fascinating topological semimetals.

ACKNOWLEDGMENTS

The authors acknowledge the support from the Ministry of Science and Technology, National Center for Theoretical Sciences, and the Academia Sinica in Taiwan. The authors also thank the National Center for High-performance Computing (NCHC) in Taiwan for the computing time.

[1] M. I. D'yakonov and V. I. Perel, Spin orientation of electrons associated with the interband absorption of light in semiconductors, Sov. J. Exp. Theor. Phys. **33**, 1053 (1971).
[2] J. E. Hirsch, Spin Hall Effect, Phys. Rev. Lett. **83**, 1834 (1999).
[3] S. Murakami, N. Nagaosa, and S.-C. Zhang, Dissipationless quantum spin current at room temperature, Science **301**, 1348 (2003).
[4] J. Sinova, D. Culcer, Q. Niu, N. A. Sinitsyn, T. Jungwirth, and A. H. MacDonald, Universal Intrinsic Spin Hall Effect, Phys. Rev. Lett. **92**, 126603 (2004).
[5] Y. K. Kato, R. C. Gossard, and D. D. Awschalom, Observation of the spin Hall effect in semiconductors, Science **306**, 1910 (2004).
[6] G. Y. Guo, Y. Yao, and Q. Niu, Ab initio Calculation of the Intrinsic Spin Hall Effect in Semiconductors, Phys. Rev. Lett. **94**, 226601 (2005).
[7] S. O. Valenzuela and M. Tinkham, Direct electronic measurement of the spin Hall effect, Nature (London) **442**, 176 (2006).
[8] H. J. Chang, T. W. Chen, J. W. Chen, W. C. Hong, W. C. Tsai, Y. F. Chen, and G. Y. Guo, Current and Strain-Induced Spin Polarization in InGaN/GaN Superlattices, Phys. Rev. Lett. **98**, 136403 (2007); Erratum: Current and Strain-Induced Spin Polarization in InGaN/GaN Superlattices, **98**, 239902(E) (2007).
[9] T. Kimura, Y. Otani, T. Sato, S. Takahashi, and S. Maekawa, Room-Temperature Reversible Spin Hall Effect, Phys. Rev. Lett. **98**, 156601 (2007).
[10] G. Y. Guo, S. Murakami, T.-W. Chen, and N. Nagaosa, Intrinsic Spin Hall Effect in Platinum: First-Principles Calculations, Phys. Rev. Lett. **100**, 096401 (2008).
[11] T. Tanaka, H. Kontani, M. Naito, D. S. Hirashima, K. Yamada, and J. Inoue, Intrinsic spin Hall effect and orbital Hall

effect in 4*d* and 5*d* transition metals, Phys. Rev. B **77**, 165117 (2008).
[12] L. Liu, C.-F. Pai, Y. Li, H.-W. Tseng, D. C. Ralph, and R. A. Buhrman, Spin-torque switching with the giant spin Hall effect of tantalum, Science **336**, 555 (2012).
[13] A. Hoffmann, Spin Hall effects in metals, IEEE Trans. Magn. **49**, 5172 (2013).
[14] J. Sinova, S. O. Valenzuela, J. Wunderlich, C. H. Back, and T. Jungwirth, Spin Hall effects, Rev. Mod. Phys. **87**, 1213 (2015).
[15] S. Cheng, Y. Xing, Q.-F. Sun, and X. C. Xie, Spin Nernst effect and Nernst effect in two-dimensional electron systems, Phys. Rev. B **78**, 045302 (2008).
[16] G. E. W. Bauer, E. Saitoh, and B. J. van Wees, Spin caloritronics, Nat. Mater. **11**, 391 (2012).
[17] S. Meyer, Y.-T. Chen, S. Wimmer, M. Althammer, T. Wimmer, R. Schlitz, S. Geprägs, H. Huebl, D. Ködderitzsch, H. Ebert, G. E. W. Bauer, R. Gross, and S. T. B. Goennenwein, Observation of the spin Nernst effect, Nat. Mater. **16**, 977 (2017).
[18] P. Sheng, Y. Sakuraba, Y.-C. Lau, S. Takahashi, S. Mitani, and M. Hayashi, The spin Nernst effect in tungsten, Sci. Adv. **3**, e1701503 (2017).
[19] N. Okuma and M. Ogata, Unconventional spin Hall effect and axial current generation in a Dirac semimetal, Phys. Rev. B **93**, 140205(R) (2016).
[20] Y. Sun, Y. Zhang, C. Felser, and B. Yan, Strong Intrinsic Spin Hall Effect in the TaAs Family of Weyl Semimetals, Phys. Rev. Lett. **117**, 146403 (2016).
[21] Y. Sun, Y. Zhang, C.-X. Liu, C. Felser, and B. Yan, Dirac nodal lines and induced spin Hall effect in metallic rutile oxides, Phys. Rev. B **95**, 235104 (2017).
[22] Y. Yen and G.-Y. Guo, Tunable large spin Hall and spin Nernst effects in the Dirac semimetals ZrXY (X = Si, Ge; Y = S, Se, Te), Phys. Rev. B **101**, 064430 (2020).
[23] D. MacNeill, G. M. Stiehl, M. H. D. Guimaraes, R. A. Buhrman, J. Park, and D. C. Ralph, Control of spin–orbit torques through crystal symmetry in WTe_2/ferromagnet bilayers, Nat. Phys. **13**, 300 (2017).
[24] S. Shi, S. Liang, Z. Zhu, K. Cai, S. D. Pollard, Y. Wang, J. Wang, Q. Wang, P. He, J. Yu, G. Eda, G. Liang, and H. Yang, All-electric magnetization switching and Dzyaloshinskii-Moriya interaction in WTe_2/ferromagnet heterostructures, Nat. Nanotechnol. **14**, 945 (2019).
[25] B. Zhao, D. Khokhriakov, Y. Zhang, H. Fu, B. Karpiak, A. Md. Hoque, X. Xu, Y. Jiang, B. Yan, and S. P. Dash, Observation of charge to spin conversion in Weyl semimetal WTe_2 at room temperature, Phys. Rev. Res. **2**, 013286 (2020).
[26] B. B. Prasad and G.-Y. Guo, Tunable spin Hall and spin Nernst effects in Dirac line-node semimetals XCuYAs (X = Zr, Hf; Y = Si, Ge), Phys. Rev. Mater. **4**, 124205 (2020).
[27] T. Ng, Y. Luo, J. Yuan, Y. Wu, H. Yang, and L. Shen, Origin and enhancement of the spin Hall angle in the Weyl semimetals LaAlSi and LaAlGe, Phys. Rev. B **104**, 014412 (2021).
[28] K. Tang, Y.-C. Lau, K. Nawa, Z. Wen, Q. Xiang, H. Sukegawa, T. Seki, Y. Miura, K. Takanashi, and S. Mitani, Spin Hall effect in a spin-1 chiral semimetal, Phys. Rev. Res. **3**, 033101 (2021).
[29] N. P. Armitage, E. J. Mele, and A. Vishwanath, Weyl and Dirac semimetals in three-dimensional solids, Rev. Mod. Phys. **90**, 015001 (2018).
[30] B. Bradlyn, J. Cano, Z. Wang, M. G. Vergniory, C. Felser, R. J. Cava, and B. A. Bernevig, Beyond Dirac and Weyl fermions: Unconventional quasiparticles in conventional crystals, Science **353**, aaf5037 (2016).
[31] G. Chang, S.-Y. Xu, B. J. Wieder, D. S. Sanchez, S.-M. Huang, I. Belopolski, T.-R. Chang, S. Zhang, A. Bansil, H. Lin, and M. Z. Hasan, Unconventional Chiral Fermions and Large Topological Fermi Arcs in RhSi, Phys. Rev. Lett. **119**, 206401 (2017).
[32] P. Tang, Q. Zhou, and S.-C. Zhang, Multiple Types of Topological Fermions in Transition Metal Silicides, Phys. Rev. Lett. **119**, 206402 (2017).
[33] D. Xiao, M.-C. Chang, and Q. Niu, Berry phase effects on electronic properties, Rev. Mod. Phys. **82**, 1959 (2010).
[34] I. V. Kavich and L. P. Shevchuk, X-ray diffraction and X-ray spectrum examinations of the Co-Si-Ge system alloys, Ukr. Fiz. Zh. (Russ. Ed.) **23**, 624 (1978).
[35] P. Demchenko, J. Kończyk, O. Bodak, R. Matvijishyn, L. Muratova, and B. Marciniak, Single crystal investigation of the new phase $Er_{0.85}Co_{4.31}Si$ and of CoSi, Chem. Met. Alloys **1**, 50 (2008).
[36] H. Takizawa, T. Sato, T. Endo, and M. Shimada, High-pressure synthesis and electrical and magnetic properties of MnGe and CoGe with the cubic B20 structure, J. Solid State Chem. **73**, 40 (1988).
[37] I. Engström and T. Johnsson, Least-squares refinement of the structure of RhSi (FeSi-type), Acta Chem. Scand. **19**, 1508 (1965).
[38] V. I. Larchev and S. V. Popova, The polymorphism of transition metal monogermanides at high pressures and temperatures, J. Less-Common Met. **87**, 53 (1982).
[39] G. Chang, B. J. Wieder, F. Schindler, D. S. Sanchez, I. Belopolski, S.-M. Huang, B. Singh, D. Wu, T.-R. Chang, T. Neupert, S.-Y. Xu, H. Lin, and M. Z. Hasan, Topological quantum properties of chiral crystals, Nat. Mater. **17**, 978 (2018).
[40] Z. Rao, H. Li, T. Zhang, S. Tian, C. Li, B. Fu, C. Tang, L. Wang, Z. Li, W. Fan, J. Li, Y. Huang, Z. Liu, Y. Long, C. Fang, H. Weng, Y. Shi, H. Lei, Y. Sun, T. Qian *et al.*, Observation of unconventional chiral fermions with long Fermi arcs in CoSi, Nature (London) **567**, 496 (2019).
[41] S. Zhong, J. E. Moore, and I. Souza, Gyrotropic Magnetic Effect and the Magnetic Moment on the Fermi Surface, Phys. Rev. Lett. **116**, 077201 (2016).
[42] F. de Juan, A. G. Grushin, T. Morimoto, and J. E. Moore, Quantized circular photogalvanic effect in Weyl semimetals, Nat. Commun. **8**, 15995 (2017).
[43] Q. Ma, S.-Y. Xu, C.-K. Chan, C.-L. Zhang, G. Chang, Y. Lin, W. Xie, T. Palacios, H. Lin, S. Jia, P. A. Lee, P. Jarillo-Herrero, and N. Gedik, Direct optical detection of Weyl fermion chirality in a topological semimetal, Nat. Phys. **13**, 842 (2017).
[44] H. Li, S. Xu, Z.-C. Rao, L.-Q. Zhou, Z.-J. Wang, S.-M. Zhou, S.-J. Tian, S.-Y. Gao, J.-J. Li, Y.-B. Huang, H.-C. Lei, H.-M. Weng, Y.-J. Sun, T.-L. Xia, T. Qian, and H. Ding, Chiral fermion reversal in chiral crystals, Nat. Commun. **10**, 5505 (2019).
[45] D. Rees, K. Manna, B. Lu, T. Morimoto, H. Borrmann, C. Felser, J. E. Moore, D. H. Torchinsky, and J. Orenstein, Helicity-dependent photocurrents in the chiral Weyl semimetal RhSi, Sci. Adv. **6**, eaba0509 (2020).
[46] Y. Sun, Q. Xu, Y. Zhang, C. Le, and C. Felser, Optical method to detect the relationship between chirality of reciprocal space chiral multifold fermions and real space chiral crystals, Phys. Rev. B **102**, 104111 (2020).

[47] V. A. Sidorov, A. E. Petrova, N. M. Chtchelkatchev, M. V. Magnitskaya, L. N. Fomicheva, D. A. Salamatin, A. V. Nikolaev, I. P. Zibrov, F. Wilhelm, A. Rogalev, and A. V. Tsvyashchenko, Magnetic, electronic and transport properties of the high-pressure-synthesized chiral magnets $Mn_{1-x}Rh_xGe$, Phys. Rev. B **98**, 125121 (2018).

[48] S. Asanabe, D. Shinoda, and Y. Sasaki, Semimetallic properties of $Co_{1-x}Fe_xSi$ solid solutions, Phys. Rev. **134**, A774 (1964).

[49] E. Skoug, C. Zhou, Y. Pei, and D. T. Morelli, High thermoelectric power factor in alloys based on CoSi, Appl. Phys. Lett. **94**, 022115 (2009).

[50] N. Kanazawa, Y. Onose, Y. Shiomi, S. Ishiwata, and Y. Tokura, Band-filling dependence of thermoelectric properties in B20-type CoGe, Appl. Phys. Lett. **100**, 093902 (2012).

[51] J. P. Perdew, K. Burke, and M. Ernzerhof, Generalized Gradient Approximation Made Simple, Phys. Rev. Lett. **77**, 3865 (1996); Erratum: Generalized Gradient Approximation Made Simple, **78**, 1396(E) (1997).

[52] P. E. Blöchl, Projector augmented-wave method, Phys. Rev. B **50**, 17953 (1994).

[53] G. Kresse and J. Hafner, *Ab initio* molecular dynamics for liquid metals, Phys. Rev. B **47**, 558 (1993).

[54] G. Kresse and J. Furthmüller, Efficient iterative schemes for *ab initio* total-energy calculations using a plane-wave basis set, Phys. Rev. B **54**, 11169 (1996).

[55] O. Jepson and O. K. Anderson, The electronic structure of h.c.p. Ytterbium, Solid State Commun. **9**, 1763 (1971).

[56] W. M. Temmerman, P. A. Sterne, G. Y. Guo, and Z. Szotek, Electronic structure calculations of high T_c materials, Mol. Simul. **4**, 153 (1989).

[57] G.-Y. Guo and T.-C. Wang, Large anomalous Nernst and spin Nernst effects in the noncollinear antiferromagnets Mn_3X (X = Sn, Ge, Ga), Phys. Rev. B **96**, 224415 (2017); Erratum: Large anomalous Nernst and spin Nernst effects in the noncollinear antiferromagnets Mn_3X (X = Sn, Ge, Ga), **100**, 169907(E) (2019).

[58] J. Qiao, J. Zhou, Z. Yuan, and W. Zhao, Calculation of intrinsic spin Hall conductivity by Wannier interpolation, Phys. Rev. B **98**, 214402 (2018).

[59] J. H. Ryoo, C.-H. Park, and I. Souza, Computation of intrinsic spin Hall conductivities from first principles using maximally localized Wannier functions, Phys. Rev. B **99**, 235113 (2019).

[60] N. Marzari, A. A. Mostofi, J. R. Yates, I. Souza, and D. Vanderbilt, Maximally localized Wannier functions: Theory and applications, Rev. Mod. Phys. **84**, 1419 (2012).

[61] G. Pizzi *et al.*, Wannier90 as a community code: New features and applications, J. Phys.: Condens. Matter **32**, 165902 (2020).

[62] See Supplemental Material at http://link.aps.org/supplemental/10.1103/PhysRevB.106.165102 for Tables S1–S3 and Figs. S1–S12, which also include Refs. [34,35] and [63].

[63] Q. S. Wu, S. N. Zhang, H.-F. Song, M. Troyer, and A. A. Soluyanov, WannierTools: An open-source software package for novel topological materials, Comput. Phys. Commun. **224**, 405 (2018).

[64] S. V. Gallego, J. Etxebarria, L. Elcoro, E. S. Tasci, and J. M. Perez-Mato, Automatic calculation of symmetry-adapted tensors in magnetic and non-magnetic materials: A new tool of the Bilbao Crystallographic Server, Acta Cryst. A **75**, 438 (2019).

[65] L. Z. Maulana, K. Manna, E. Uykur, C. Felser, M. Dressel, and A. V. Pronin, Optical conductivity of multifold fermions: The case of RhSi, Phys. Rev. Res. **2**, 023018 (2020).

[66] H. L. Wang, C. H. Du, Y. Pu, R. Adur, P. C. Hammel, and F. Y. Yang, Scaling of Spin Hall Angle in 3d, 4d, and 5d Metals from $Y_3Fe_5O_{12}$/Metal Spin Pumping, Phys. Rev. Lett. **112**, 197201 (2014).

[67] G. de la Flor, D. Orobengoa, E. Tasci, J. M. Perez-Mato, and M. I. Aroyo, Comparison of structures applying the tools available at the Bilbao Crystallographic Server, J. Appl. Cryst. **49**, 653 (2016).

[68] J.-C. Tung and G.-Y. Guo, High spin polarization of the anomalous Hall current in Co-based Heusler compounds, New J. Phys. **15**, 033014 (2013).